



HAL
open science

Morphological properties of superclusters of galaxies

M. V. Costa-Duarte, L. Sodr , F. Durret

► **To cite this version:**

M. V. Costa-Duarte, L. Sodr , F. Durret. Morphological properties of superclusters of galaxies. Monthly Notices of the Royal Astronomical Society, 2011, 411, pp.1716-1726. 10.1111/j.1365-2966.2010.17803.x . insu-03646029

HAL Id: insu-03646029

<https://insu.hal.science/insu-03646029>

Submitted on 21 Apr 2022

HAL is a multi-disciplinary open access archive for the deposit and dissemination of scientific research documents, whether they are published or not. The documents may come from teaching and research institutions in France or abroad, or from public or private research centers.

L'archive ouverte pluridisciplinaire **HAL**, est destin e au d p t et   la diffusion de documents scientifiques de niveau recherche, publi s ou non,  manant des  tablissements d'enseignement et de recherche fran ais ou  trangers, des laboratoires publics ou priv s.

Morphological properties of superclusters of galaxies

M. V. Costa-Duarte,^{1*} L. Sodr e Jr,¹ and F. Durret^{2,3†}

¹*Instituto de Astronomia, Geof sica e Ci ncias Atmosf ricas, USP, R. do Mat o 1226, 05508-090 S o Paulo, Brazil*

²*Institut d'Astrophysique de Paris, UPMC Universit  Paris 06, UMR 7095, F-75014 Paris, France*

³*CNRS, UMR 7095, Institut d'Astrophysique de Paris, F-75014 Paris, France*

Accepted 2010 October 1. Received 2010 September 24; in original form 2010 June 1

ABSTRACT

We studied superclusters of galaxies in a volume-limited sample extracted from the Sloan Digital Sky Survey Data Release 7 and from mock catalogues based on a semi-analytical model of galaxy evolution in the Millennium Simulation. A density field method was applied to a sample of galaxies brighter than $M_r = -21 + 5 \log h_{100}$ to identify superclusters, taking into account selection and boundary effects. In order to evaluate the influence of the threshold density, we have chosen two thresholds: the first maximizes the number of objects (D1) and the second constrains the maximum supercluster size to $\sim 120 h^{-1}$ Mpc (D2). We have performed a morphological analysis, using Minkowski Functionals, based on a parameter, which increases monotonically from filaments to pancakes. An anticorrelation was found between supercluster richness (and total luminosity or size) and the morphological parameter, indicating that filamentary structures tend to be richer, larger and more luminous than pancakes in both observed and mock catalogues. We have also used the mock samples to compare supercluster morphologies identified in position and velocity spaces, concluding that our morphological classification is not biased by the peculiar velocities. Monte Carlo simulations designed to investigate the reliability of our results with respect to random fluctuations show that these results are robust. Our analysis indicates that filaments and pancakes present different luminosity and size distributions.

Key words: cosmology: large-scale structure of Universe – galaxies: clusters: general – methods: data analysis.

1 INTRODUCTION

It is well known that galaxies are not randomly distributed in the Universe, with high-density regions being observed as large-scale structures and low-density regions as voids. Under the current Λ cold dark matter (Λ CDM) cosmological paradigm, the evolution of these structures started in the early Universe from primordial density fluctuations just after inflation, leading to the observed cosmic web. At very large scales, of tens of Mpc, clusters, groups and even pairs or isolated galaxies are disposed in very large associations, sometimes of filamentary or planar structure. These associations are the largest non-virialized structures in the Universe: superclusters of galaxies. Their dynamical future is still uncertain, but in a dark energy dominated Universe most of them may evolve to *island universes*, single, isolated and highly concentrated mass clumps (Araya-Melo et al. 2009).

The study of very large scale structures started with de Vaucouleurs (1953), who identified a high-density region in the galaxy distribution on the sky, nowadays known as the local supercluster. Abell (1958) also helped to unveil large scales through his catalogue of clusters of galaxies identified in the Palomar Observatory photographic plates; he defined superclusters as clusters of galaxies. Larger surveys were carried out and, as a consequence, the distribution of galaxies in the local Universe could be studied in detail. The Harvard Center for Astrophysics survey measured the redshift of a sample of galaxies brighter than 14.5 (Huchra et al. 1983), showing the filamentary distribution of galaxies, with galaxy clusters at the connection of the filaments. These redshifts allowed to constrain the cosmological model. Indeed, Efstathiou, Sutherland & Maddox (1990) showed, from the analysis of large-scale galaxy clustering in the *IRAS* survey, that a cosmological constant was required to explain the galaxy distribution in the framework of the CDM model.

The data derived from redshift surveys later allowed to study the properties of individual superclusters, like Pisces-Cetus (Tully 1988) and Shapley (Proust et al. 2006), as well as those of the whole population of superclusters, revealing that they tend to have

*E-mail: mvcduarte@astro.iag.usp.br

†This file has been amended to highlight the proper use of L^AT_EX 2_ε code with the class file.

an elongated morphology and extensions up to $\sim 100 h^{-1}$ Mpc (Bahcall & Soneira 1984). Recent works reveal extensions up to $110\text{--}130 h^{-1}$ Mpc (Pandey et al. 2010). The study of superclusters highly benefited from the 2dF Galaxy Redshift Survey (2dFGRS) (Colless, Dalton & Maddox 2001) and the Sloan Digital Sky Survey (SDSS) (Abazajian et al. 2009).

Indeed, more complete studies of large-scale structures were possible using these large-redshift surveys. Jaan Einasto's group used the 2dFGRS data to generate a catalogue of superclusters (Einasto et al. 2007a, hereinafter E07a). They also compared observed superclusters to simulated ones (Einasto et al. 2007b, hereinafter E07b) and studied the spectral properties of galaxies within superclusters (Einasto et al. 2007c). Their main results indicate that the overall properties of simulated and observed superclusters present good agreement with each other, but their luminosity and multiplicity (number of galaxies) distributions seem to be different. Additionally, they found that galaxy morphology in superclusters depends on their richness, with rich superclusters presenting an early-type fraction slightly higher than poor superclusters. In another series of papers (Einasto et al. 2007d,e), these authors have studied the richest superclusters identified in the observations. Comparing the clumpiness of simulated and observed superclusters, they conclude that the clumpiness of galaxies in simulations is different from that observed (Einasto et al. 2007d) and that the global and local environments are quite important for galaxy morphology and star formation activity (Einasto et al. 2007e).

Since superclusters are non-virialized structures, they present a variety of morphologies (West 1989; Plionis, Valdarnini & Jing 1992). Several studies have used shape statistics (Sahni, Sathyaprakash & Shandarin 1998) and Minkowski Functionals (MFs) (Mecke, Buchert & Wagner 1994) to determine topological and geometrical properties useful for morphological analysis. The SDSS and PSCz (Saunders et al. 2000) superclusters seem to have a prevalence of filamentary structures (Basilakos 2003), as well as a concordance with the Λ CDM model of large-scale structure formation (Basilakos et al. 2001, hereinafter B01). A comparison of observed and simulated superclusters showed that simulated superclusters are very similar to those observed, but the number density of very luminous superclusters seems to be higher in observations than in simulations (Einasto et al. 2006, hereinafter E06).

Morphological studies suggest that galaxies are found in two distinct classes of structures at very large scales: filaments and pancakes. Using the shapefinder technique (Sahni et al. 1998), B01 applied this approach to distinguish between these two classes using the so-called shape-spectrum. Further works used filament features to constrain the galaxy clustering, since the bias parameter is also sensitive to filamentarity (Bharadwaj & Pandey 2004). Using galaxy luminosities and colours, Pandey & Bharadwaj (2006) found a dependence between galaxy properties and filamentarity, proposing a scenario where elliptical galaxies are predominantly in dense regions, while spiral galaxies are distributed along filaments. A strong spatial alignment between clusters and host superclusters in large filaments was found in N -body simulations (Basilakos et al. 2006; Lee & Edvard 2007).

Here we present a study of supercluster morphologies through the study of the galaxy distribution in volume-limited samples extracted from the SDSS Data Release 7 (SDSS-DR7; Abazajian et al. 2009). We use a kernel-based density field method to identify the superclusters and MFs to quantify their shape.

This paper is organized as follows. Section 2 presents the data used here as well as our method to deal with selection effects. In Section 3, we describe the kernel-based density field method

used to identify superclusters as well as the criteria to classify enhanced regions as superclusters, taking into account the selection and boundary effects. In Section 4, the morphological classification is described and in Section 5, we discuss the morphology of observed and simulated superclusters. Finally, in Section 6, we summarize the main conclusions of this paper. In Appendix A, we discuss the sensitivity of our supercluster identification and morphological analysis to the adopted kernel.

When necessary, distances were calculated assuming the following cosmology: $\Omega_m = 0.3$, $\Omega_\Lambda = 0.7$ and Hubble parameter $H_0 = 100 h_{100}^{-1} \text{ km s}^{-1} \text{ Mpc}^{-1}$.

2 DATA

The analysis presented in this paper is based on a volume-limited galaxy sample extracted from the SDSS-DR7 (Abazajian et al. 2009). We have considered galaxies with measured radial velocities and with absolute magnitudes in the r band brighter than $-21 + 5 \log h$ in the redshift range $0.04 \leq z \leq 0.155$. Absolute magnitudes were calculated with k -corrections obtained with the code `KCORRECT` v4.1.4 and with a specific SDSS package provided by Blanton & Roweis (2007). Since superclusters may extend over several degrees on the sky, we have considered only galaxies within stripes 10–37 to assure a large continuous area on the sky. The total number of galaxies selected is 120 013.

In Section 5, we will compare some of our results with numerical simulations. For this we have used simulated light-cones produced by Croton et al. (2006), based on a semi-analytic galaxy evolution model applied to the output of the Millennium Simulation (Springel et al. 2005). We have selected the four light-cones with parameters suited for the SDSS: SDSS_SAcone_012_000, SDSS_SAcone_012_100, SDSS_SAcone_120_000 and SDSS_SAcone_201_000. Each covers an area of $60 \times 30 \text{ deg}^2$ and the simulated galaxies were selected following the same criteria as adopted in the selection of our volume-limited sample of SDSS galaxies. The number of simulated galaxies selected in the four light-cones is 99 850.

3 THE DENSITY FIELD METHOD

Superclusters are sometimes defined as large-scale overdensity regions in the galaxy distribution (de Vaucouleurs 1953). Adopting this definition, the density field method represents a convenient way to identify these structures (e.g. B01; E07a). In this section, we describe how we define the density field of a sample of galaxies.

3.1 The density field

First, using the equatorial coordinates (α, δ) and the redshift z of each galaxy, we calculated its Cartesian coordinates as

$$\begin{aligned} x &= d_c \cos(\delta) \cos(\alpha) \\ y &= d_c \cos(\delta) \sin(\alpha) \\ z &= d_c \sin(\delta) \end{aligned} \quad (1)$$

where $d_c(z)$ is the comoving distance of the galaxy.

The luminosity density of the galaxy distribution, $D(r)$, is calculated through the kernel approach. At a certain point \mathbf{r} in space, it is given by

$$D(r) = \sum_i K(|\mathbf{r} - \mathbf{r}_i|, \sigma) L_i W_i(\mathbf{r}_i), \quad (2)$$

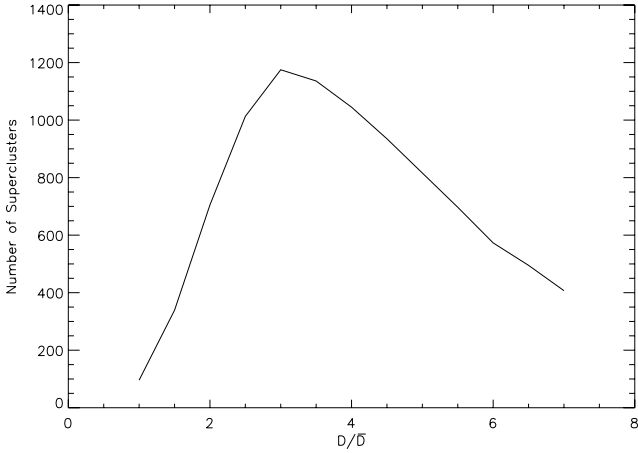


Figure 1. Number of superclusters as a function of the threshold density (in units of the mean density).

where $K(r, \sigma)$ is the kernel used to smooth the galaxy distribution, L_i is the luminosity of the i th galaxy (at position r_i) and $W_i(r_i)$ is a weight, which takes into account selection effects (discussed in the next section).

We adopt here Epanechnikov’s kernel, which minimizes the asymptotic mean integrated squared error (e.g. Silvermann 1986) and is defined as

$$K(r, \sigma) = \begin{cases} \frac{3}{4} [1 - (r/\sigma)^2] & r \leq \sigma \\ 0 & r > \sigma \end{cases} \quad (3)$$

Here σ is the smoothing parameter. We have adopted $\sigma = 8 h^{-1}$ Mpc. The reason is that the number density of galaxies in our sample (see the next section) is $\bar{n} = 2.1 \times 10^{-3} (h^{-1} \text{Mpc})^{-3}$, corresponding to a mean distance between galaxies of $\sim 8 h^{-1}$ Mpc. As shown later, this choice leads to a density field relatively insensitive to peculiar velocities. The density field is sampled in a three-dimensional grid with cells of side $l_{\text{cell}} = 4 h^{-1}$ Mpc.

To identify structures in the density field, it is necessary to define a density threshold to separate high-density regions (e.g. superclusters) from low-density regions (e.g. voids). In this way, we have rejected all grid points below the threshold. Afterwards, a friends-of-friends algorithm was used to connect nearby high-density grid points, assigning them to single objects. The linking-length used is equal to the diagonal of the cell grid, that is, $l_{\text{for}} = \sqrt{3} l_{\text{cell}} \simeq 7 h^{-1}$ Mpc. Only objects with more than 10 galaxies and volume larger than two grid cells, $V_{\text{min}} = 2(l_{\text{cell}})^3 = 128 (h^{-1} \text{Mpc})^3$, will be considered in the analysis (E07a).

Note that about 0.3 per cent of the DR7 imaging footprint area is marked as holes. In these regions, we have used bilinear interpolation to obtain the density field, considering only grid points, at a given redshift, more distant than $8 h^{-1}$ Mpc from the hole borders. Since the area occupied by the holes is small, and most of the holes are in low-density regions, it can be verified that this procedure has a negligible impact on our results.

There is no natural value for the threshold density. In Fig. 1, we present the number of structures (hereinafter called superclusters) as a function of the threshold in units of mean density (\bar{D}), computed with the selection function discussed in Section 3.2. For low threshold density values, percolation links distinct structures and consequently the number of superclusters is low. At high threshold values, only high-density objects are identified, also resulting in a low number of structures. In this work, we have adopted two distinct values for the threshold density. The first one, $D_{\text{thresh}} = 3 \times \bar{D}$

(hereinafter D1), is the value, which maximizes the number of superclusters. The second one, $D_{\text{thresh}} = 6 \times \bar{D}$ (hereinafter D2), was chosen such that the largest superclusters present an extension of $\sim 120 h^{-1}$ Mpc, as adopted by E07a. This length consists of the diagonal of the box, which contains all galaxies of the supercluster, that is, $l = \sqrt{\Delta x^2 + \Delta y^2 + \Delta z^2}$.

Two important features of superclusters can be defined here: their richness and total luminosity. The richness can be written as

$$R = \sum_i^{N_{\text{gal}}} W_i, \quad (4)$$

where N_{gal} represents the number of galaxies of the supercluster and W_i is the selection effect correction of the i th galaxy. The total supercluster luminosity – actually the expected luminosity above the magnitude limit – is defined as

$$L_{\text{tot}} = \sum_i^{N_{\text{gal}}} L_i W_i, \quad (5)$$

where L_i represents the luminosity of the i th galaxy.

It is worth mentioning that our results are not too sensitive to the choice of the smoothing kernel. We present in Appendix A a summary of results obtained with a truncated Gaussian kernel, showing that our estimates of supercluster parameters are indeed very robust.

3.2 A model for the selection function

The selection function aims at correcting for galaxies brighter than our magnitude limit that, for a reason or another, were not included in the sample.

Indeed, our magnitude-limited sample is affected by incompleteness due to fibre collisions in the spectroscopic survey. Consequently, although the nominal magnitude limit of the SDSS Main Galaxy Sample (MGS) is $m_r = 17.77$, not all galaxies brighter than this limit were observed. There is a minimum distance between fibre allocations by the SDSS spectrographs of about 55 arcsec (Strauss et al. 2002) and some galaxies within the MGS photometric limits do not have spectroscopy, because they are closer than 55 arcsec to a galaxy to which a fibre was allocated. This spectroscopic incompleteness depends on the apparent magnitude, since fainter galaxies are more affected. This is shown in Fig. 2, which presents the fraction of galaxies with spectroscopy as a function of the apparent magnitude m_r .

The spectroscopic incompleteness leads to a radial selection effect, since galaxies with higher apparent magnitude tend to be at higher redshifts. Since in this case the shot-noise increases with distance, the coupling between this radial effect and a constant smoothing parameter introduces an additional distortion in the density field (Gaztanaga & Yokoyama 1993; Seljak, Hamaus & Desjacques 2009). This bias leads to an overestimation of the density with increasing redshift (B01).

To deal with these effects, we have adopted a simple model for the selection function, with two components. The first one depends on the apparent magnitude [$S_1(m_r)$] and the second one on the redshift or comoving distance [$S_2(d_c)$]. The selection function is thus defined as

$$S(m_r, d_c) = S_1(m_r) S_2(d_c) \quad (6)$$

and is related to the weight W as

$$W = S(m_r, d_c)^{-1}.$$

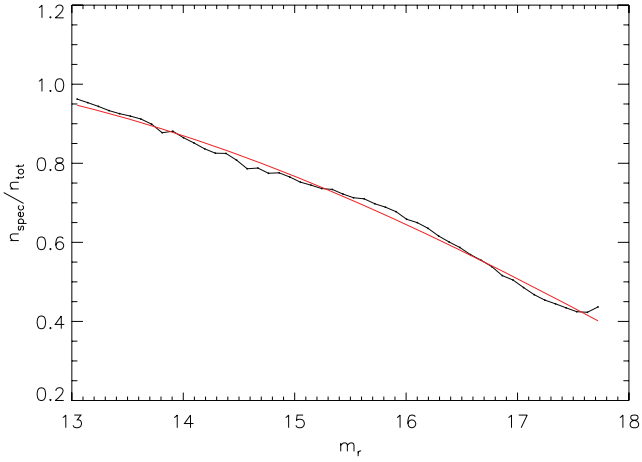


Figure 2. Fraction of galaxies with observed spectra as a function of apparent r -band magnitude in the range $13.0 < m_r < 17.77$. The red line represents the fourth-order polynomial fitted to the observed trend.

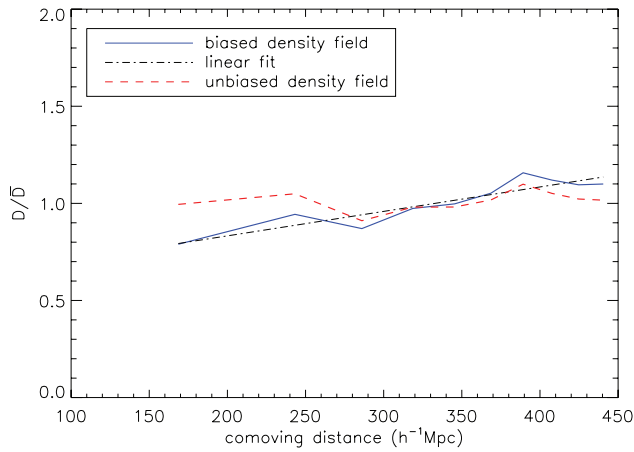


Figure 3. The blue continuous line shows the mean density in equal volume regions as a function of the comoving distance when only the magnitude selection effect is taken into account. The slight dependence of the density with distance shows evidence for a radial bias. The blue dot-slash-dotted line is the linear fit adopted to model this radial bias and the red dashed line represents the mean density after correcting the density field by the magnitude and radial selection effects.

The apparent magnitude component can be defined as $S_1(m_r) = n_{\text{spec}}/n_{\text{tot}}$ and we model the trend seen in Fig. 2 with a fourth-order polynomial:

$$S_1(m_r) = 0.588605 - 1.941834m_r + 0.419142m_r^2 - 0.029956m_r^3 + 0.000724m_r^4. \quad (7)$$

To estimate the radial component of the selection function, we, initially, calculated the mean of the density field grid points in 10 regions with the same volume, taking into account only the apparent magnitude incompleteness [i.e. assuming $S_2(d_c) = 1$]. As shown in Fig. 3, the mean density of each region increases with redshift, reflecting the bias mentioned above. However, a comparison with fig. 3 of B01 indicates that the effect here is significantly less severe in our volume-limited sample than in magnitude-limited samples. To correct for this effect, we model the dependence of the mean density with the comoving distance as $S_2(d_c) = ad_c + b$ with $a = 0.0025$ and $b = 0.1565$ for distances in Mpc. Taking $S_2(d_c)$

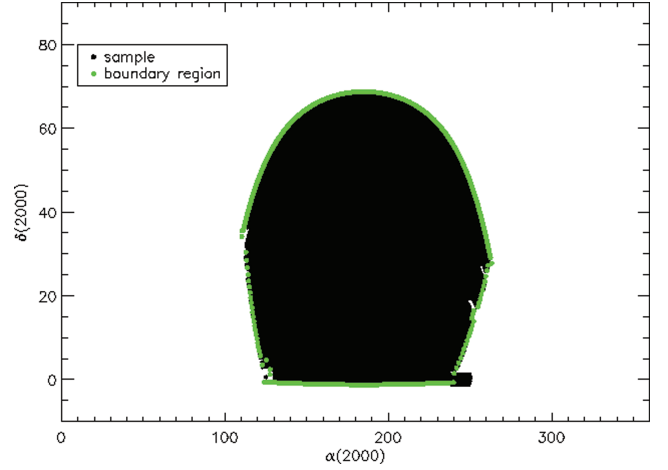


Figure 4. Region occupied by our sample on the sky (in black). Green dots represent the boundary of the region.

into account, the radial trend in the mean value of the density field disappears, as shown in Fig. 3.

3.3 Boundary effects

Due to the large sizes of superclusters and the limited volume of our galaxy sample, care should be taken to avoid boundary effects that can affect the analysis described in the following sections.

With this aim, we considered only structures where all galaxies have comoving transversal distances from any volume boundary larger than $\sigma = 8 h^{-1}$ Mpc. Fig. 4 shows the region occupied by our initial sample (in black) as well as its boundary points (in green). Superclusters in the region with $240^\circ < \alpha < 253^\circ$ and $-2^\circ < \delta < +2^\circ$ were excluded from our sample to avoid boundary effects. Excluding superclusters at the boundary, our final supercluster sample has 880 structures above the threshold D1 and 409 structures above the threshold D2. Their main properties are shown in Table 1.

4 MORPHOLOGICAL DESCRIPTION OF SUPERCLUSTERS

Since superclusters of galaxies are not virialized structures, they present a large variety of shapes. In this section, we present the shapefinder method, which we adopted to describe the morphology of these structures. First, we discuss the ellipsoidal model to describe the structures and then we use MFs to obtain a morphological parameter.

4.1 The ellipsoidal model

A simple description of the three-dimensional morphology of a body can be obtained through its best-fitting triaxial ellipsoid. This model has eight free parameters: three for the centroid of the structure, two for its orientation and three for the semi-axes a_1 , a_2 and a_3 .

The parameters of the ellipsoid can be inferred from the inertia tensor, that is, the matrix of second-order moments of particle positions:

$$I_{ij} = \sum_k L_k W_k x_i^k x_j^k, \quad (8)$$

where x_i^k represents the i th coordinate of the k th galaxy with respect to the object centroid. The matrix I_{ij} can be diagonalized and the

Table 1. Statistics for observed and simulated superclusters for the two threshold densities. The table shows the number of superclusters classified as filaments (N_f), pancakes (N_p), the mean number density (\bar{n}_{SC}) of superclusters and median values for total luminosity, richness and K_1/K_2 . For simulated superclusters, we also present our results in the position space.

Threshold	Sample	N_f	N_p	$\bar{n}_{SC}(10^{-5} h^3 \text{ Mpc}^{-3})$	$\log(L_{\text{tot}}/L_{\odot})$	$\log(R)$	K_1/K_2
D1 (velocity space)	SDSS-DR7	436	444	1.55	11.82	1.39	1.00
	012.000	74	83	1.02	12.01	1.58	1.02
	012.100	70	75	0.94	12.02	1.60	1.01
	120.000	86	86	1.11	11.99	1.55	1.00
	201.000	76	81	1.02	12.01	1.60	1.04
D2 (velocity space)	SDSS-DR7	204	212	0.74	12.07	1.64	1.01
	012.000	31	27	0.37	12.29	1.85	0.92
	012.100	29	29	0.37	12.37	1.90	1.00
	120.000	45	23	0.44	12.28	1.83	0.88
	201.000	29	28	0.37	12.30	1.86	0.99
D1 (position space)	012.000	98	90	1.22	11.97	1.55	0.97
	012.100	85	85	1.10	12.03	1.60	1.01
	120.000	82	109	1.24	12.00	1.57	1.08
	201.000	84	89	1.06	11.96	1.55	0.99
D2 (position space)	012.000	31	27	0.38	12.24	1.78	1.07
	012.100	29	29	0.37	12.33	1.89	1.03
	120.000	34	27	0.40	12.24	1.78	0.97
	201.000	29	32	0.39	12.21	1.77	1.00

diagonal elements are proportional to the best-fitting ellipsoid semi-axes (e.g. Plionis, Barrow & Frenk 1991; Jang-Condell & Hernquist 2001; Kolokotronis, Basilakos & Plionis 2002):

$$\begin{aligned}
 I_1 &= \frac{\sum_i L_i W_i}{5} (a_2^2 + a_3^2), \\
 I_2 &= \frac{\sum_i L_i W_i}{5} (a_1^2 + a_3^2), \\
 I_3 &= \frac{\sum_i L_i W_i}{5} (a_1^2 + a_2^2). \tag{9}
 \end{aligned}$$

Solving the system of equations above, the three semi-axes are determined, with the assumption that $a_1 \geq a_2 \geq a_3$.

4.2 Minkowski Functionals

MFs represent an important tool to describe structures and objects, since they characterize their geometry. We follow here the formalism of Sahni et al. (1998), which uses ellipsoidal models for the morphological description of the objects.

Having as input parameters the semi-axes a_1 , a_2 and a_3 obtained in the previous section, we can determine, for an object or isodensity contour, four parameters: the volume (V), the surface (S), the integrated mean curvature (C) and the integrated Gaussian curvature (\mathcal{G}), also called *genus*.

The parametric equation for an ellipsoid with semi-axes a_1 , a_2 and a_3 can be written as

$$\mathbf{r}(\theta, \phi) = a_1(\sin \theta \cos \phi) \hat{\mathbf{i}} + a_2(\sin \theta \sin \phi) \hat{\mathbf{j}} + a_3(\cos \theta) \hat{\mathbf{k}}. \tag{10}$$

We now define

$$E = \mathbf{r}_{\theta} \cdot \mathbf{r}_{\theta},$$

$$F = \mathbf{r}_{\theta} \cdot \mathbf{r}_{\phi},$$

$$G = \mathbf{r}_{\phi} \cdot \mathbf{r}_{\phi},$$

$$L = \mathbf{r}_{\theta\theta} \cdot \mathbf{n},$$

$$M = \mathbf{r}_{\theta\phi} \cdot \mathbf{n},$$

$$N = \mathbf{r}_{\phi\phi} \cdot \mathbf{n},$$

where

$$r_{\phi} = \partial \mathbf{r} / \partial \phi,$$

$$r_{\theta} = \partial \mathbf{r} / \partial \theta,$$

$$r_{\phi\phi} = \partial^2 \mathbf{r} / \partial \phi^2,$$

$$r_{\theta\theta} = \partial^2 \mathbf{r} / \partial \theta^2,$$

$$r_{\theta\phi} = \partial^2 \mathbf{r} / \partial \theta \partial \phi.$$

The vector \mathbf{n} represents the unit vector perpendicular to the surface and is defined as

$$\mathbf{n} = \mathbf{r}_{\theta} \times \mathbf{r}_{\phi} / |\mathbf{r}_{\theta} \times \mathbf{r}_{\phi}|.$$

The four geometrical quantities can then be written as

$$S = \iint \sqrt{EG - F^2} d\theta d\phi, \tag{11}$$

$$C = \iint \frac{k_1 + k_2}{2} dS, \tag{12}$$

$$\mathcal{G} = \frac{-1}{4\pi} \iint k_1 k_2 dS, \tag{13}$$

$$V = \frac{4}{3} \pi a_1 a_2 a_3. \tag{14}$$

The principal curvatures of the ellipsoid are k_1 and k_2 , and the sum and product of these quantities are, respectively,

$$k_1 + k_2 = \frac{EN + GL - 2FM}{EG - F^2}, \tag{15}$$

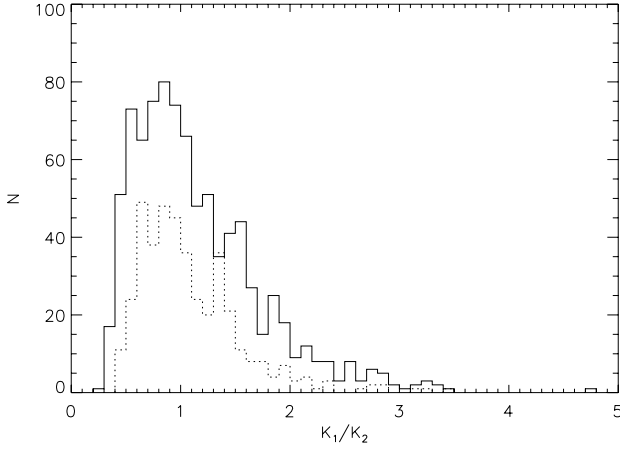


Figure 5. The histogram shows the distribution of K_1/K_2 for SDSS superclusters considering D1 (solid line) and D2 (dotted line). Both distributions present a median value around unity.

and

$$k_1 k_2 = \frac{LN - M^2}{EG - F^2}. \quad (16)$$

Three parameters are introduced, H_1 , H_2 and H_3 , which have dimensions of length: $H_1 = 3V/S$, $H_2 = S/C$ and $H_3 = C/4\pi$. Combinations of these parameters provide two important *shapefinders*, K_1 (planarity) and K_2 (filamentarity), which can, respectively, be expressed as

$$K_1 = \frac{H_2 - H_1}{H_2 + H_1} \quad (17)$$

and

$$K_2 = \frac{H_3 - H_2}{H_3 + H_2}. \quad (18)$$

The vector $\mathbf{K} = (K_1, K_2)$ has an amplitude and direction, which determine the shape of a certain three-dimensional surface. An ideal pancake-like object presents one dimension, which is much smaller than the others, so $H_1 \ll H_2 \simeq H_3$ and consequently $\mathbf{K} \simeq (1, 0)$. For an ideal filament, $H_1 \gg H_2 \simeq H_3$ and so $\mathbf{K} \simeq (0, 1)$. Considering surfaces like ribbons, the shapefinders have three distinct dimensions, that is, $H_1 \ll H_2 \ll H_3$ and $\mathbf{K} \simeq (\alpha, \alpha)$ with $\alpha < 1$. It is worth mentioning that, for a sphere, $H_1 = H_2 = H_3$ and hence $\mathbf{K} = (0, 0)$.

This formalism can be used to classify objects with different shapes, so we consider the following two morphologies:

- (i) Objects with $K_1/K_2 > 1$ are classified as pancakes.
- (ii) Objects with $0 \leq K_1/K_2 \leq 1$ are classified as filaments.

The range of K_1/K_2 for ribbons is somewhat arbitrary ($K_1/K_2 \simeq 1$), so we decided to exclude this morphology from our classification. The shape statistics K_1/K_2 , through the so-called ‘shape spectrum’, was first applied to astronomy by B01.

Fig. 5 shows the distribution of the morphological parameter K_1/K_2 . Table 1 presents some statistical properties of the supercluster morphologies, considering the two threshold densities discussed in Section 3.1.

5 RESULTS AND DISCUSSION

In this section, we investigate how overall properties of superclusters, like their richness and total luminosity, correlate with their

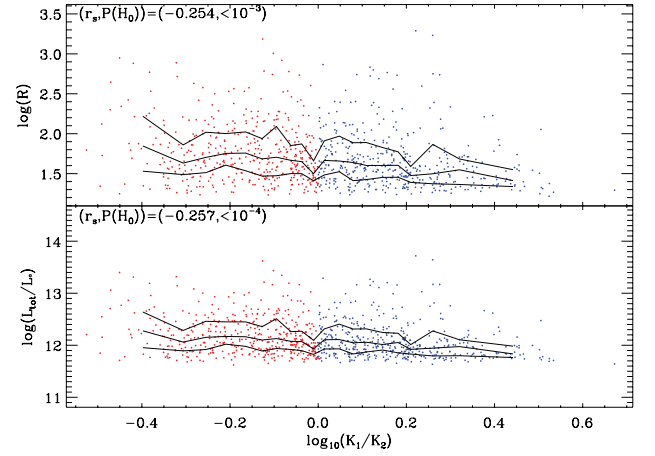


Figure 6. Richness (top panel) and total luminosity (bottom panel) of SDSS superclusters as a function of the morphological parameter K_1/K_2 for the density threshold D1. The median and quartiles of the distribution are shown.

morphological properties. We also repeat the analysis for structures extracted from numerical simulations, with the main objective of comparing the supercluster properties in the position and velocity spaces.

5.1 SDSS superclusters

Fig. 5 and Table 1 indicate that we have essentially the same number of objects classified as filaments or pancakes in our sample, for the two density thresholds discussed here. We found 436 filaments and 444 pancakes for the threshold D1 and 204 filaments and 212 pancakes for the threshold D2. Hence, our result does not confirm previous works (e.g. B01), where a prevalence of objects classified as filaments was found.

In order to investigate relations between morphology and properties of superclusters, the Spearman rank-order correlation coefficient, r_s , was used to measure possible correlations (Press et al. 2007). We have also computed the two-sided significance level of the null hypothesis of absence of correlation (or anticorrelation), $P(H_0)$; a small value of $P(H_0)$ is indicative of strong correlation (or anticorrelation).

Fig. 6 shows the richness and total luminosity of SDSS superclusters as a function of the morphological parameter K_1/K_2 , considering the threshold D1. The lines represent the median and quartiles for each bin of K_1/K_2 . Despite the large scatter, there is a significant trend between richness (and consequently total luminosity) and the morphological parameter K_1/K_2 . In both cases, we found $r_s \simeq -0.25$ and $P(H_0) < 10^{-4}$, showing that filamentary structures tend to be richer and more luminous than pancakes. A similar behaviour is found for the threshold D2, with a correlation coefficient $r_s \simeq -0.25$ and $P(H_0) < 10^{-4}$ for both richness and total luminosity. These results indicate that the trends of richness and total luminosity with the morphological parameter are not strong but are statistically significant.

We have also compared the luminosity distributions of filaments and pancakes through the Kolmogorov–Smirnov (K–S) test (Fig. 7). We conclude that their distributions are statistically distinct, presenting a K–S probability lower than 10^{-3} that the cumulative luminosity distributions of filaments and pancakes are drawn from the same distribution. A similar result is achieved using the threshold D2, in this case with a probability $< 10^{-3}$. Indeed, Fig. 7 suggests that the luminosity distribution of filaments is significantly broader than

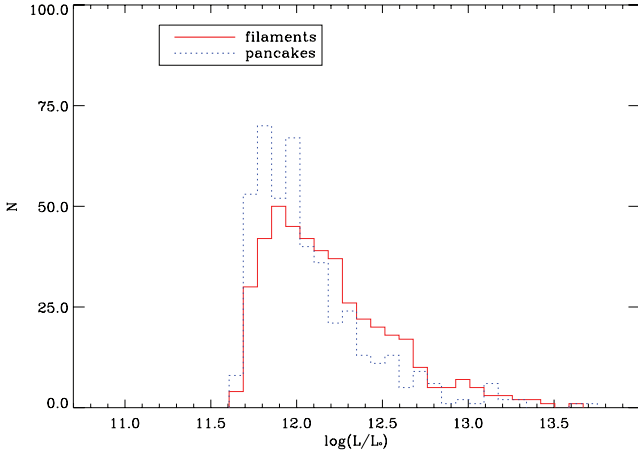


Figure 7. Observed luminosity distribution of filaments (continuous red histogram) and pancakes (dotted blue histogram), for the density threshold D1.

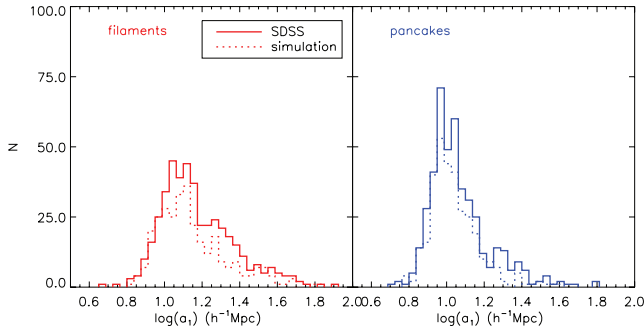


Figure 8. Distribution of the semimajor axis resulting from the ellipsoidal fitting to the structures. Left-hand panel: filaments; right-hand panel: pancakes. Dotted lines correspond to the distributions obtained from the superclusters extracted from the numerical simulations described in Section 5.2. Results for the density threshold D1.

that of pancakes, resulting in a higher number of filaments at high luminosities, in agreement with Fig. 6. A similar trend for superclusters classified as filaments to be richer and consequently more luminous had already been reported by E07b.

Considering now only the brightest structures, those with $\log(L/L_{\odot}) > 12.5$, we may note the prevalence of filaments over pancakes: 60.4 and 39.6 per cent, respectively, for the threshold D1, and 62.5 and 37.5 per cent, respectively, for the threshold D2.

Fig. 8 shows the distribution of the semimajor axis resulting from the ellipsoidal fitting to the structures. Filaments and pancakes have different sizes, as demonstrated also by Fig. 9, with filaments comprising most of the largest superclusters.

5.2 Analysis of simulated superclusters

We have repeated the above analysis for the four mock SDSS catalogues described in Section 2, applying the same procedures as described in Sections 3 and 4.

Table 1 shows the number of superclusters identified in the simulations, classified as filaments or pancakes, as well as the mean number density and median values of richness, total luminosity and K_1/K_2 for each sample of superclusters and threshold densities. Comparing the median values of total luminosity and richness from both threshold densities, slightly higher values are found in the

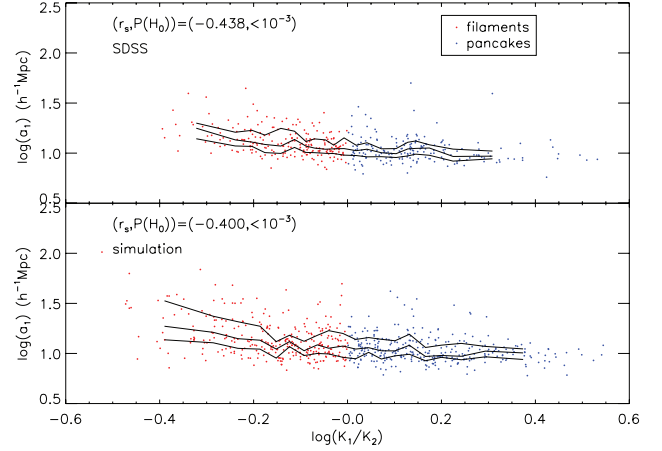


Figure 9. Semimajor axis resulting from the ellipsoidal fitting to the structures as a function of the morphological parameter K_1/K_2 for the density threshold D1. The median and quartiles of the distribution are shown. Top panel: SDSS sample. Bottom panel: superclusters extracted from the numerical simulations described in Section 5.2.

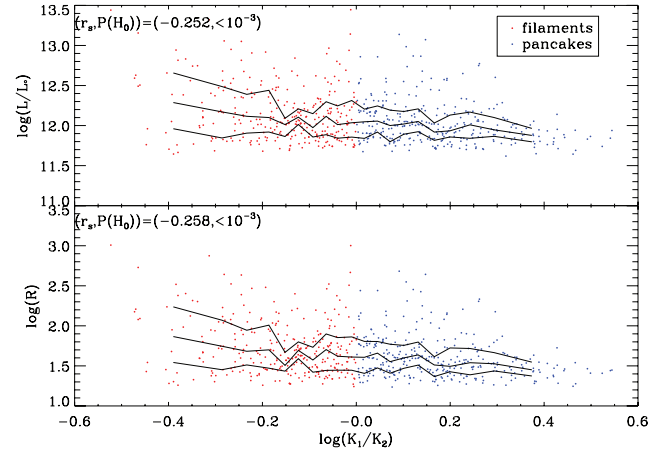


Figure 10. Richness (top panel) and total luminosity (bottom panel) of superclusters extracted from numerical simulations as a function of the morphological parameter K_1/K_2 for the density threshold D1. The median and quartiles of the distribution are shown.

threshold D2, because only richer and more luminous superclusters are identified using this threshold, increasing the median values.

The same behaviour of observed richness and total luminosity with the morphological parameter K_1/K_2 is present in the simulations. Fig. 10 shows the relation between richness, total luminosity and K_1/K_2 for the superclusters extracted from the simulations with the density threshold D1. The value of the Spearman coefficient is $r_s = -0.25$ and $P(H_0) < 10^{-4}$ considering the threshold D1, and $r_s = -0.25$ and $P(H_0) < 10^{-4}$ for the threshold D2. This anticorrelation between richness, total luminosity and K_1/K_2 in the mock catalogues is very similar to that obtained for observed superclusters (Fig. 6), indicating a good agreement between simulations and observations.

Peculiar velocities may have an important influence on supercluster identification. The observed redshift of extragalactic objects has a component produced by the Hubble flow plus a peculiar velocity component due to gravitational interactions. Consequently, there is a difference between measured distances in velocity and position spaces, which produces some features in the velocity space,

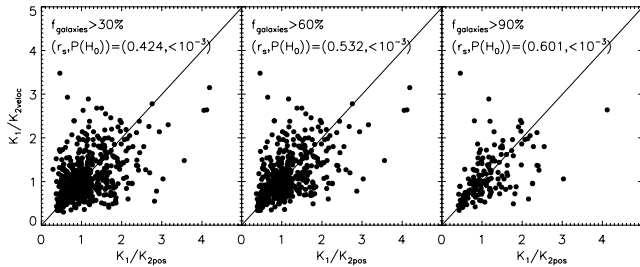


Figure 11. Comparison between the values of the morphological parameter of simulated superclusters identified in the velocity and position spaces. Each panel corresponds to different limits in the fraction of galaxies in common (f_g) in structures identified in the velocity and position spaces.

such as the fingers-of-god and the Kaiser effect (e.g. Jackson 1972; Bahcall, Soneira & Burgett 1986; Kaiser 1987). In order to study the influence of peculiar velocities on supercluster identification and morphology, we identified superclusters in the mock samples of Croton et al. (2006) using two sets of redshifts available in the simulations: the first one including peculiar velocities (velocity space) and the second without them (position space). The influence of peculiar velocities on the identification and morphological classification of superclusters can be studied by comparing the properties of simulated superclusters in both spaces. Table 1 also presents the main features of simulated supercluster samples identified in velocity and position spaces. Qualitatively, results are similar for the density thresholds D1 and D2.

Due to peculiar velocities, galaxies associated to a structure in position space may or may not be associated to the same structure identified in velocity space. In order to compare the morphologies of superclusters identified in both spaces, superclusters from position space were associated to ones from velocity space, according to the percentage of galaxies (f_g) in common (30, 60 and 90 per cent). Fig. 11 shows $K_1/K_{2\text{veloc}}$ versus $K_1/K_{2\text{pos}}$ for different percentages of galaxies in common. In all cases, there is a significant correlation between the morphological parameter measured in both spaces, despite the large scatter, which increases as f_g increases. Interestingly, there is no significant bias in the morphological parameter measured in velocity space compared with the values measured in position space. This is actually due to the high values of the smoothing parameter adopted here (see Section 3).

As another test of how morphology is distorted in redshift space, we have considered galaxies in superclusters identified in redshift space and compared the morphology they trace in both velocity and position spaces. Fig. 12 shows the distribution of K_1/K_2 in velocity and position-spaces in this case. The median values of K_1/K_2 are similar ($K_1/K_{2\text{veloc}} = 1.01$ and $K_1/K_{2\text{pos}} = 1.04$) in both spaces. A K–S test indicates that the two distributions are consistent with each other. Hence, this test also suggests that peculiar velocities are not important for our morphology measurements.

We now consider the luminosity distribution of superclusters identified in the velocity and position spaces in the mock catalogues. Fig. 13 shows this distribution for filaments and pancakes for the density threshold D1. For each morphological class, the distributions in both spaces are quite similar, as confirmed by the K–S test. It is worth mentioning that these distributions in velocity space resemble very much the observed distributions (Fig. 10). This is confirmed by a K–S test comparison of the filament and pancake distributions with K–S probability equal to 0.85 and 0.42, respectively, for the null hypothesis that the data were drawn from the

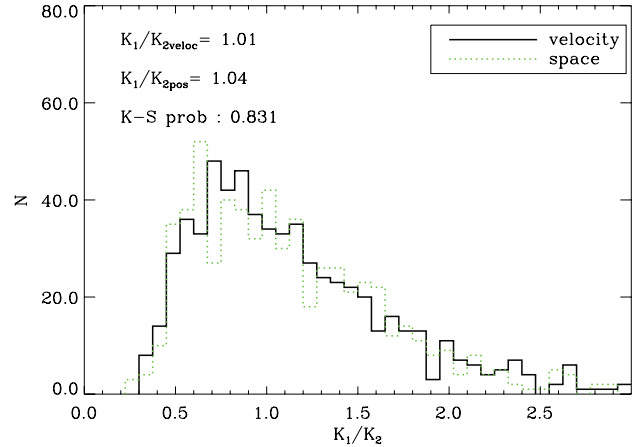


Figure 12. Distribution of the morphological parameter of superclusters identified in velocity (black) and position (green) spaces. The median values of K_1/K_2 (top left-hand panel) are similar and the K–S test shows that the distributions are consistent with each other.

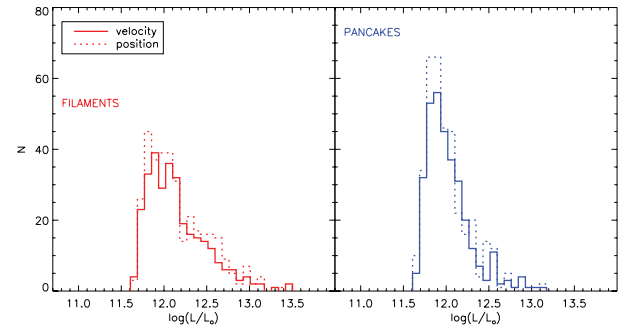


Figure 13. Luminosity distributions of filaments and pancakes identified in the mock catalogues, in velocity and position spaces, for the threshold D1.

same distribution. Both probabilities show that the distributions are not statistically distinct.

The trend of the semimajor axis (a_1) of the ellipsoidal fitting of observed and simulated superclusters with the morphological parameter shown in Fig. 9 provides an indication that the largest structures tend to be filamentary. The trend is very similar for the observed and simulated structures.

Our results indicate that simulated and observed superclusters present similar properties. This is also the case for the luminosity distributions of observed and simulated superclusters, as can be seen in Figs 7 and 13. However, E06 have found an absence of very luminous superclusters in simulations compared with observations. Indeed, a comparison between the observed and mock samples shows that objects brighter than $\log(L/L_\odot) > 12.5$ are at least twice more frequent in the observations than in the mock samples.

Additionally, by comparing the luminosity distribution of superclusters classified as filaments and pancakes, we have noted that these classes have very different luminosity distributions. Since filaments tend to be richer and more luminous than pancakes, it is fair to suggest that these two morphological classes represent different evolutive dynamical stages of the large-scale structure, with pancakes possibly evolving to filaments.

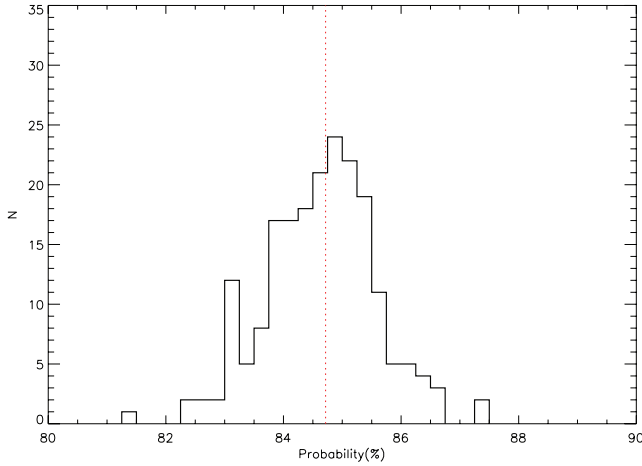


Figure 14. Distribution of the probability of identifying real superclusters for the density threshold D1. The median value (red dotted line) is around 85 per cent.

5.3 Statistical reliability of supercluster identification

Our method of supercluster identification is strongly dependent on the threshold density and on the smoothing parameter. Thus, it is necessary to verify its robustness by checking what fraction of our detections are expected to be real or just statistical noise.

To investigate the expected number of random clumps, we follow the approach proposed by Basilakos (2003). We ran a large number (200) of Monte Carlo simulations where we randomized the equatorial coordinates of the galaxies, keeping their comoving distances and the sample boundaries in order to preserve the selection function. Since this randomization destroys the SDSS clustering, the structures identified in each simulation will be due to statistical noise. The probability of identifying real superclusters in our sample through this procedure is then

$$P = 1 - \frac{N_{\text{rand}}}{N_{\text{SDSS}}}, \quad (19)$$

where N_{rand} is the number of structures identified in the randomized samples and N_{SDSS} is the number of structures identified in our original SDSS sample. A probability close to 1 means that the number of spurious objects produced by our supercluster identification method is small.

This analysis was performed for the same threshold densities as in Section 3.1. Fig. 14 shows the resulting probability distribution obtained with the threshold D1, presenting a median probability P of around 85 per cent. For the threshold D2, the median probability is higher than 99.8 per cent. Fig. 15 compares the luminosity distribution of our D1 SDSS superclusters with that obtained from the simulations. The result clearly indicates that most random structures have luminosities significantly lower than those of the SDSS superclusters. This result is also noted by comparing the median values of the SDSS and random luminosity distributions.

The same morphological analysis as described in Section 4 was applied to the structures identified in the Monte Carlo simulations. No trends were found between the total luminosity or richness and the morphological parameter K_1/K_2 , indicating that the results displayed in Fig. 6 are indeed real and not produced by random fluctuations or by the selection function of the sample.

Another test of robustness of the main trends identified in this work can be done by considering only structures with total luminosities larger than $10^{12} L_{\odot}$, since our Monte Carlo simulations

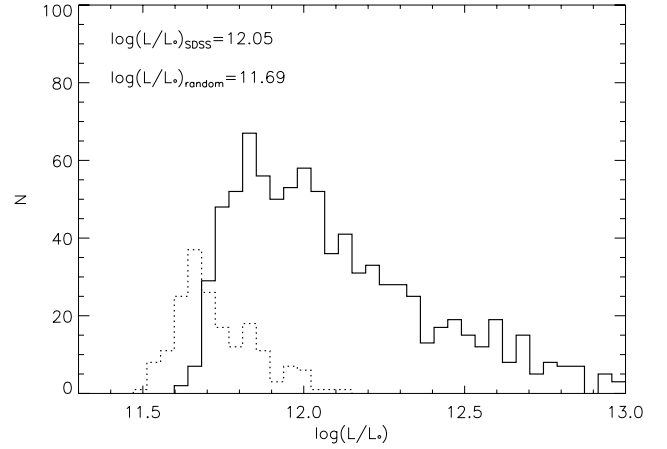


Figure 15. Luminosity distributions of SDSS superclusters (continuous line) and random superclusters (dotted line) for the density threshold D1. The median of logarithmic values (top left-hand panel) shows that random superclusters present significantly lower luminosities than SDSS superclusters.

indicate that the expected number of spurious structures in this case is only ~ 3.7 per cent. All our previous results are confirmed.

6 SUMMARY AND CONCLUSIONS

We have selected a volume-limited sample of galaxies from the SDSS in order to identify galaxy superclusters, determine their morphologies and investigate some of their features. Our SDSS sample contains galaxies with $M_r < -21$ in the redshift range $0.04 < z < 0.155$ and covers stripes 10–37. We have also analysed simulated light-cones based on a semianalytic galaxy evolution model applied to the output of the Millenium Simulation (Croton et al. 2006) to confront theory and observations and to examine the role of some systematic effects.

Superclusters were identified by the density field method with an Epanechnikov kernel, taking into account selection and boundary effects. By comparing the results obtained with this kernel with those obtained with a truncated Gaussian kernel, we show that the results are not strongly dependent on the kernel choice. The kernel smoothing parameter and the dimension of the density field cell were chosen as $\sigma = 8 h^{-1}$ Mpc and $l_{\text{cell}} = 4 h^{-1}$ Mpc, respectively. Two threshold densities were chosen to evaluate their influence on supercluster identification and morphology. The first maximizes the number of structures (D1) and the second is chosen by limiting the size of the largest superclusters to $\sim 120 h^{-1}$ Mpc (D2). We found that, at least qualitatively, our results do not depend on the density threshold used. Each supercluster is characterized by its richness and total luminosity, as well as by a morphological parameter determined through MFs, which allows their classification as filaments or pancakes.

Following E07b, we have found significant correlations of the morphological parameter K_1/K_2 with richness and total luminosity in both the observed and the mock supercluster catalogues, indicating that filaments tend to be richer and consequently more luminous than pancakes.

To evaluate the influence of peculiar velocities on supercluster morphology, we have used mock catalogues to examine structures identified in the velocity and position spaces. We conclude that peculiar velocities do not play a significant role in our results,

probably due to the large kernel smoothing length adopted in this work.

We have found a trend between supercluster total luminosity (or richness) and morphology, with filaments being in the mean more luminous than pancakes. A similar behaviour was found by analysing mock catalogues. The analysis of Monte Carlo simulations of randomized galaxy distributions indicates that these trends are real and are not produced by random fluctuations or selection effects.

Finally, we compared the luminosity and size distributions of filaments and pancakes. We have found that they are significantly different, with filaments presenting a broader distribution of sizes and luminosities. Again, similar results were obtained by the analysis of the mock catalogues, showing that filaments and pancakes represent distinct morphological classes of superclusters in the Universe. Also, since filaments tend to be richer, more luminous and larger than pancakes, it is plausible to think that pancakes evolve towards filaments.

ACKNOWLEDGMENTS

We are grateful to the referee, Spyros Basilakos, for his constructive and very helpful comments. MVC-D thanks CAPES for a scholarship that allowed him to develop this project. LS acknowledges FAPESP and CNPq for their support to his research. FD and LS acknowledge the support of the Brazilian-French collaboration CAPES/Cofecub (444/04). We also wish to thank the team of the SDSS for their dedication to a project, which has made this work possible.

REFERENCES

- Abazajian K. N. et al., 2009, *ApJS*, 182, 543
 Abell G. O., 1958, *ApJS*, 3, 211
 Araya-Melo P. A., Reisenegger A., Meza A., van de Weygaert R., Dunner R., Quintana H., 2009, *MNRAS*, 399, 97
 Bahcall N. A., Soneira R. M., 1984, *ApJ*, 277, 27
 Bahcall N. A., Soneira R. M., Burgett W. S., 1986, *ApJ*, 311, 15
 Basilakos S., 2003, *MNRAS*, 344, 602
 Basilakos S., Plionis M., Rowan-Robinson M., 2001, *MNRAS*, 323, 47 (B01)
 Basilakos S., Plionis M., Yepes G., Gottlöber S., Turchaninov V., 2006, *MNRAS*, 365, 539
 Bharadwaj S., Pandey B., 2004, *ApJ*, 615, 1
 Blanton M. R., Roweis S., 2007, *AJ*, 133, 734
 Colless M., Dalton G., Maddox S., 2001, *MNRAS*, 328, 1039
 Croton D. J. et al., 2006, *MNRAS*, 365, 11
 de Vaucouleurs G., 1953, *AJ*, 58, 30
 Efstathiou G., Sutherland W. J., Maddox S. J., 1990, *Nat*, 348, 705
 Einasto J. et al., 2006, *A&A*, 459, L1 (E06)
 Einasto J. et al., 2007a, *A&A*, 462, 811 (E07a)
 Einasto J. et al., 2007b, *A&A*, 462, 397 (E07b)
 Einasto M. et al., 2007c, *A&A*, 464, 815
 Einasto M. et al., 2007d, *A&A*, 476, 697
 Einasto M. et al., 2007e, preprint (arXiv:0706.1126)
 Gaztanaga E., Yokoyama J., 1993, *ApJ*, 403, 450
 Huchra J., Davis M., Latham D., Tonry J., 1983, *ApJS*, 52, 89
 Jackson J. C., 1972, *MNRAS*, 130, 1P
 Jang-Condell H., Hernquist L., 2001, *ApJ*, 548, 68
 Kaiser N., 1987, *MNRAS*, 227, 1
 Kolokotronis V., Basilakos S., Plionis M., 2002, *MNRAS*, 331, 1020
 Lee J., Evrard A. E., 2007, *ApJ*, 657, 30
 Mecke K. R., Buchert T., Wagner H., 1994, *A&A*, 288, 697
 Pandey B., Bharadwaj S., 2006, *MNRAS*, 372, 827

- Pandey B., Kulkarni G., Bharadwaj S., Souradeep T., 2010, *MNRAS*, preprint (arXiv:1009.2223)
 Plionis M., Barrow J. D., Frenk C. S., 1991, *MNRAS*, 249, 662
 Plionis M., Valdarnini R., Jing Y. P., 1992, *ApJ*, 398, 12
 Press W. H., Teukolsky S. A., Vetterling W. T., Flannery B. P., 2007, *Numerical Recipes: The Art of Scientific Computing*. Cambridge Univ. Press, Cambridge
 Proust D. et al., 2006, *The Messenger*, 124, 30
 Sahni V., Sathyaprakash B. S., Shandarin S. F., 1998, *ApJ*, 495, L5
 Saunders W. et al., 2000, *MNRAS*, 317, 55
 Seljak U., Hamaus N., Desjacques V., 2009, *Phys. Rev. Lett.*, 103, 9
 Silvermann B. W., 1986, *Density Estimation for Statistics and Data Analysis*. Chapman and Hall, London, New York
 Springel V. et al., 2005, *Nat*, 435, 629
 Strauss M. A., Weinberg D. H., Lupton R. H., Narayanan V. K., Annis J., Bernardi M., Blanton M., Burles S., 2002, *AJ*, 124, 1810
 Tully R. B., 1988, in Audouze J., Pelletan M.-C., Szalay S., eds, *Proc. IAU Symp. 130, The Pisces-Cetus Supercluster Complex*. Reidel Publishing Co., Dordrecht, p. 243
 West M. J., 1989, *ApJ*, 347, 610

APPENDIX A: THE INFLUENCE OF THE SMOOTHING KERNEL ON SUPERCLUSTER PROPERTIES

The kernel in equation (2) plays a fundamental role in the density field calculation and therefore it is important to verify how sensitive our results are to the kernel choice. We address this point by comparing supercluster properties obtained with the Epanechnikov kernel with their properties obtained with a truncated Gaussian kernel, defined as

$$K(r, \sigma) = \frac{1}{2\pi} e^{-r^2/2\sigma^2}, \quad (\text{A1})$$

with a cut-off at 3σ .

For this exercise, the density field was calculated as described in Section 3.1, but with a smoothing parameter $\sigma = 2.4 h^{-1} \text{Mpc}$ for the truncated Gaussian model. This value leads to 1038 superclusters for the threshold D1 with luminosities similar to those discussed in Section 5.1, as shown in Fig. A1. A similar result is obtained by comparing the richness of superclusters obtained with the two kernels.

In order to compare the structures obtained with these kernels, we have matched the two supercluster catalogues by assuming that

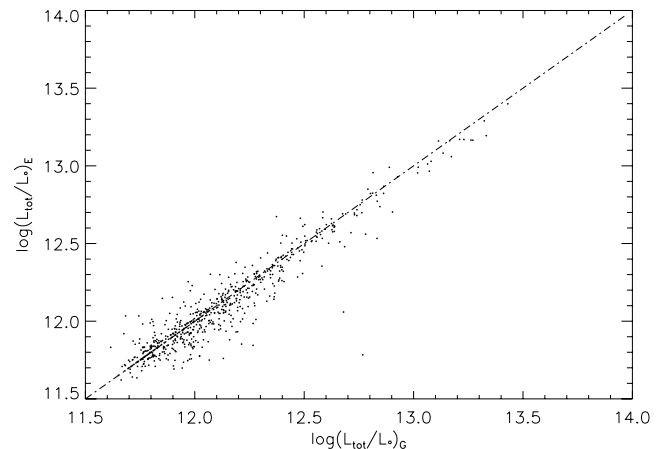


Figure A1. Comparison between the total luminosity of superclusters identified using the Gaussian $[\log(L/L_{\odot})_G]$ and Epanechnikov $[\log(L/L_{\odot})_E]$ kernels with parameters described in the text.

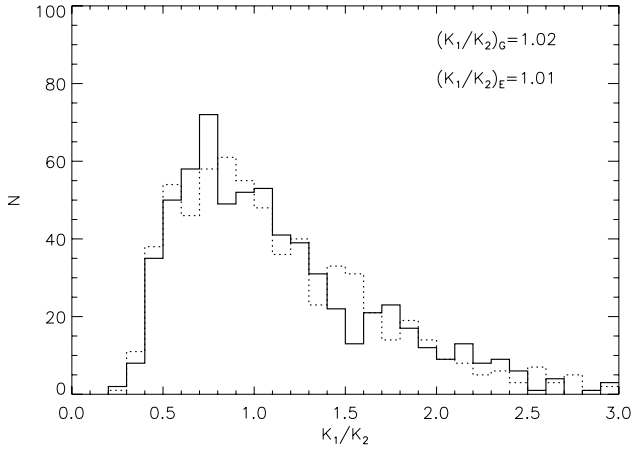


Figure A2. Distribution of the morphological parameter K_1/K_2 for superclusters identified using the Epanechnikov (dotted line) and Gaussian (continuous line) kernels. At the top right-hand panel, we show the median values of each distribution.

the distance between the object centre-of-mass in both catalogues is lower than $8 h^{-1}$ Mpc. In this way, we have identified 368 objects in common.

In Fig. A2, we compare the distributions of the morphological parameter K_1/K_2 obtained with the two kernels. The distributions have similar medians and the K–S test did not distinguish them. The same trends present in Fig. 6 were found using the Gaussian kernel, with a correlation coefficient $r_s \simeq -0.18$ and $P(H_0) < 10^{-3}$ for both luminosity and richness. Similar results are obtained with the threshold D2. We conclude that the trends described in the text are actually robust with respect to the kernel choice, as far as sensible kernels are used.

This paper has been typeset from a $\text{\TeX}/\text{\LaTeX}$ file prepared by the author.